

A Traveling-Wave Parametric Amplifier With Integrated Diplexers

C. Denney,^{1,2} K. Genter,^{1,3} K. Cicak,¹ J. D. Teufel,^{1,3}
 J. Aumentado,¹ F. Lecocq,^{1,3,*} and M. Malnou^{1,3,†}

¹*National Institute of Standards and Technology,
 325 Broadway, Boulder, CO 80305, USA*

²*Colorado School of Mines, 1500 Illinois St, Golden, CO, 80401, USA*

³*University of Colorado, 2000 Colorado Ave., Boulder, CO 80309, USA*

(Dated: March 16, 2026)

Traveling-Wave Parametric Amplifiers (TWPAs) are ubiquitous in superconducting circuit readout, providing high gain with near-quantum-limited noise performance across a wide bandwidth. Their operation, however, relies on a strong microwave pump tone that is typically delivered using off-chip passive components, such as directional couplers or diplexers. These external elements add loss, increase system complexity, and limit scalability. Here, we present a traveling-wave parametric amplifier that incorporates on-chip input and output diplexers for pump routing. This co-fabricated architecture offers a compact and scalable solution for superconducting-circuit readout.

I. INTRODUCTION

Parametric amplifiers have become indispensable for measuring signals interacting with superconducting circuits, including the microwave resonators used in qubit and sensor architectures [1–10]. Often used as the first stage of amplification, they provide high gain with minimal added noise [11–14]. Among them, traveling-wave parametric amplifiers (TWPAs) have become increasingly popular over the past decade. Compared to resonant parametric amplifiers, the TWPA’s inherently broader bandwidth and higher power handling allows them to read out multiple resonators simultaneously, greatly improving practicality in multiplexed readout architectures [9, 10].

Yet, existing TWPAs still rely on a substantial amount of external microwave hardware that impede scalability [9–16]. In conventional implementations, the amplifier chip must be surrounded by off-chip components that route and manage the strong pump tone required for parametric gain. Reciprocal elements such as directional couplers or diplexers are used to inject the pump into the signal path and to filter it

out at the output. In addition, nonreciprocal devices such as isolators are typically placed between the TWPA and the device under test to suppress back-action. These input/output (I/O) networks, assembled from connectorized commercial components, degrade the readout chain’s noise performance and increase the overall system footprint.

In this article, we present a four-wave-mixing Josephson TWPA with superconducting diplexers co-fabricated on chip at both its input and output. These diplexers introduce two additional physical ports that enable local pump delivery and pump extraction without external microwave hardware. They also separate the signal and idler bands into distinct off-chip paths, eliminating the requirement for the upstream readout chain to also be matched at the idler frequency. This diplexed TWPA (D-TWPA) delivers about 13 dB of gain across a 2 GHz signal-amplification bandwidth. Within this band and for this gain, the average system-added noise is 2 quanta, as determined from a noise measurement employing a shot-noise tunnel junction [13, 14, 17–19].

* florent.lecocq@nist.gov

† maxime.malnou@nist.gov

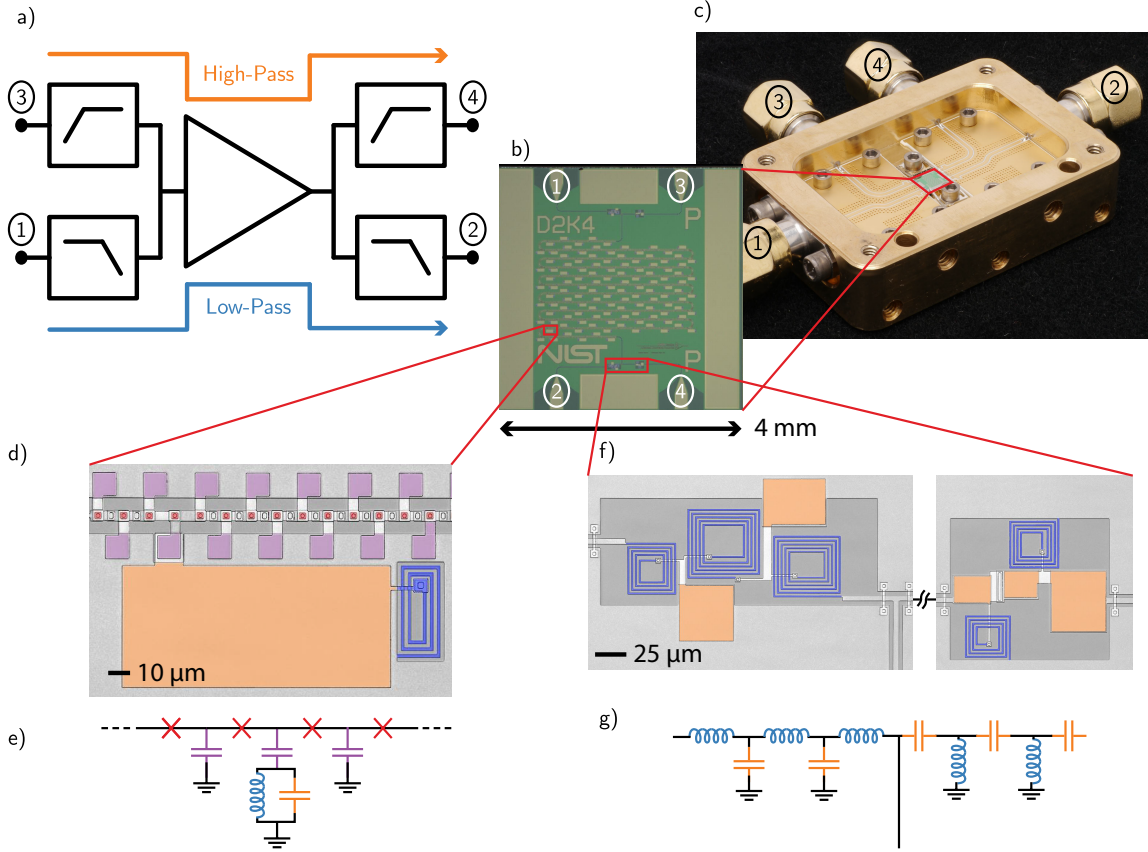


FIG. 1. An overview of the D-TWPA integrated layout. (a) The TWPA is connected to the common port of a diplexer on each end. (b) The resulting chip has four microwave ports, along with the packaged device (c). The phase-matching resonator (d) and the lumped-element diplexers (f) are shown in false color micrographs, along with their corresponding equivalent schematics, (e) and (g) respectively.

II. DESIGN

The active part of the D-TWPA consists of a standard $50\ \Omega$ nonlinear artificial transmission line formed by series Josephson-junction inductors shunted to ground through capacitors, see Fig. 1b. This amplifier employs four-wave mixing (4WM) where the pump frequency ω_p lies between the signal (ω_s) and idler (ω_i) frequencies, satisfying $2\omega_p = \omega_s + \omega_i$ [20]. To achieve phase matching between the pump, signal and idler propagating waves, an LC resonator is periodically inserted in the shunt branch [21], see

Fig. 1d,e. The resonator is designed with a resonance at 8.7 GHz, slightly above the desired pump frequency at 8.5 GHz, and its low mode impedance ($Z_{\text{rpm}} \approx 15\ \Omega$) minimizes the width of the generated stopband, which is unusable for amplification.

For practical operation, we aim to separate the low-frequency signal band from the higher-frequency band that contains both the pump and idler tones. We therefore designed a pair of identical lumped-element diplexers whose common ports connect directly to the TWPA, see Fig. 1a. This configuration creates a four-port device

(two low-frequency ports and two high-frequency ports), as shown in Fig. 1c. Each diplexer is constructed from fifth-order Chebyshev low-pass and high-pass filters (see Fig. 1g). Their compact footprint (approximately $300\ \mu\text{m} \times 300\ \mu\text{m}$, see Fig. 1f), much smaller than the TWPA itself, allows them to be readily integrated on chip without significantly increasing the chip area.

The diplexer crossover frequency is chosen so that the signal band lies below 8 GHz, ensuring compatibility with a standard C-band readout chain. Conversely, the TWPA idler-band output is routed to a dedicated port that can be terminated in a cryogenic matched load mounted on the TWPA package, eliminating the need for the rest of the chain to provide a good match at these higher frequencies. The common ports of the diplexers are well matched across the entire operating band.

The TWPA and diplexers were co-fabricated on a single chip using niobium trilayer Josephson junctions (critical current $I_c \simeq 5\ \mu\text{A}$), and parallel-plate capacitors employing a low-loss amorphous silicon dielectric ($\tan \delta \simeq 4 \times 10^{-4}$) [15, 22].

III. SCATTERING MEASUREMENTS

We first characterized the device’s driven response at cryogenic temperatures. Microwave switches mounted on each of the four ports allowed us to compare the TWPA’s transmission to a through reference in both the signal and idler bands (see the full characterization setup in appendix B).

Figure 2a shows the transmission amplitude through the low- and high-frequency ports of the unpumped TWPA, referenced to the through-cable calibration. The thickness of the dielectric layer was measured to be 13% thicker than the value used for simulation, which caused the diplexer crossover and the resonant phase matching feature to shift to 8.5 GHz and 9.2 GHz respectively. The insertion loss remains below 3 dB up to 14 GHz, owing to the low-loss amorphous-silicon dielectric.

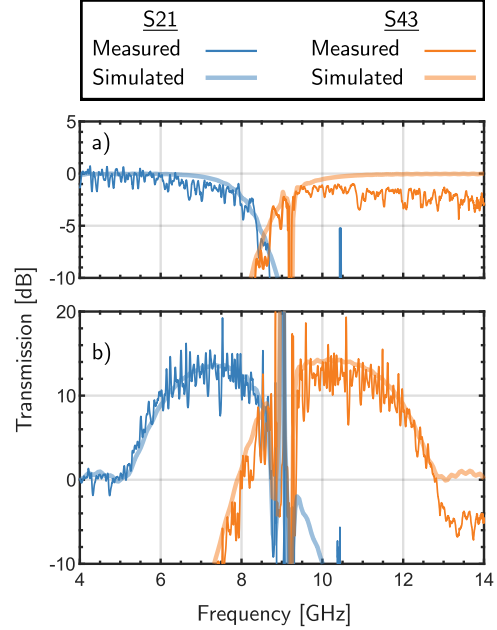


FIG. 2. Gain and insertion loss measurements relative to a through reference. With the pump off (a) the crossover of the diplexer appears at 8.5 GHz, and the resonant phase matching feature is just above 9 GHz. (b) The gain profile with a pump optimized for noise performance (9.06 GHz and $-76.8\ \text{dBm}$) is measured through both S_{21} (blue curve) and S_{43} (orange curve). Predicted scattering from simulations neglecting internal loss and early junction switching are shown in light blue and orange, in good agreement with the measurements.

Figure 2b shows the calibrated transmission amplitude through the low- and high-frequency ports of the device (S_{21} and S_{43} respectively) when the pump is applied through the high-frequency input port. The TWPA generates broadband gain of about 13 dB between 6 and 8 GHz in the signal band, and between 10 and 12 GHz in the idler band. We attribute the $\sim 5\ \text{dB}$ gain ripples to impedance mismatches that arise between the TWPA chip and its packaging when it is pumped (see appendix A). Although a maximum broadband gain of $\sim 20\ \text{dB}$ can be obtained at higher pump power, the noise performance degrades at these higher gains [23, 24].

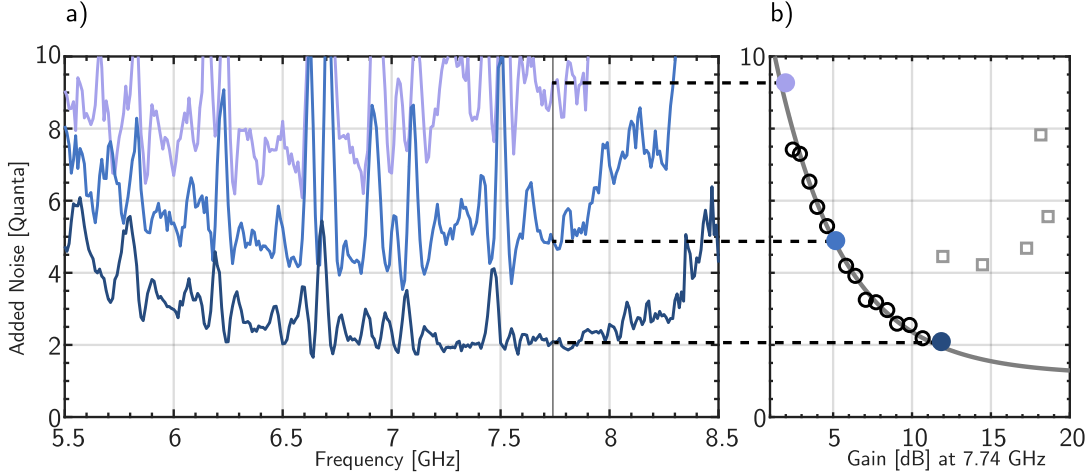


FIG. 3. Measurement of the chain-added noise where the TWPA is the first amplifier. (a) The chain-added noise between 5.5 GHz and 8.5 GHz is shown for three different TWPA gains increasing from light purple to dark blue. (b) Focusing on a frequency bin centered at 7.74 GHz, the chain-added noise decreases as the TWPA gain increases, until it increases again at higher pump powers. These measurements (squares) were excluded from the fit used to extract N_{TWPA} .

We compared these transmission measurements to the steady-state response of an equivalent lumped-element model of the TWPA and diplexers, simulated in the time domain using WRSpice [25]. The pump power of -76.8 dBm used in the simulation was chosen to match our estimate of the pump power incident on the TWPA’s high-frequency input in the experiment (see appendix C). As shown in Fig. 2, this model accurately reproduces both the unpumped (a) and pumped (b) transmission responses, except for internal losses which were not modeled.

IV. NOISE CHARACTERIZATION

We extracted the broadband added noise of the chain using a Y-factor measurement, with a shot-noise tunnel junction (SNTJ) serving as a calibrated noise source [13, 14, 17–19]. The microwave switch connected to the TWPA’s low-frequency input can toggle between the continuous-wave probe tone and the SNTJ, allowing us to perform scattering and noise measurements under identical conditions *in situ*.

The output noise N_{out} was recorded on a spectrum analyzer as a function of the chain’s input noise N_{in} generated by the SNTJ.

To extract the chain-added noise N_{add} (in units of quanta) we fit the measured N_{out} as a function of N_{in} using [14]

$$N_{\text{out}} = G_{\text{tot}}(N_{\text{in}} + N_{\text{add}}) \quad (1)$$

Where G_{tot} , the gain of the readout chain, is a fit parameter. The added noise includes the low-gain correction

$$N_{\text{add}} = \frac{G_{\text{TWPA}} - 1}{2G_{\text{TWPA}}} + N_{\text{ex}}, \quad (2)$$

where G_{TWPA} is the gain of the TWPA alone. We assume a 14 mK idler temperature that contributes to 1/2 quantum of noise since the diplexer allows the SNTJ to illuminate only the signal input (and not the idler). The term N_{ex} represents the excess of noise above the quantum limit of $N_{\text{add}} = 1/2$ attained at high gain.

Figure 3a shows the extracted N_{add} as a function of frequency for various pump powers. As the power (and gain) increases, N_{add} decreases,

reaching an average minimum of 2 quanta between 6 and 8 GHz. However, once the gain exceeds roughly 13 dB, the added noise begins to rise again as shown in Fig. 3b, illustrating the gain–noise tradeoff typically seen in TWPA’s [23, 24].

By measuring the chain added noise, N_{add} , as a function of G_{TWPA} we can separate the noise contribution of the TWPA itself, N_{TWPA} , from that of the remaining amplification chain, N_{rem} , using

$$N_{\text{add}} = N_{\text{TWPA}} + \frac{N_{\text{rem}}}{G_{\text{TWPA}}}. \quad (3)$$

Fitting N_{add} as a function of G_{TWPA} (known from thru-calibrated S parameters during the same cooldown) yields $N_{\text{TWPA}} = 1.17 \pm 0.14$ quanta 7.74 GHz, see Fig. 3b.

V. CONCLUSION

We have presented a TWPA with integrated input and output diplexers, eliminating the need for external circuitry to deliver and filter the microwave pump. This architecture improves the practicality of the amplifier and reduces its overall footprint, making it well suited for deployment in large-scale quantum computing systems. The diplexed TWPA achieves performance on par with existing devices in both gain and added noise. Looking forward, such on-chip diplexers can be combined with the various recent advances in TWPA technology [24, 26, 27] that have led to higher gain and power handling, lower ripples, and reduced added noise.

Appendix A: Amplifier packaging

The amplifier is clipped directly to a brass housing (see Fig. 1c) alongside printed circuitboards (PCBs) that facilitate the transition from the coaxial connector to the wirebonds. Toward the chip, single-stub matching was used to compensate the wire-bond inductance. Toward the coaxial connector, the overall width of the coplanar waveguide (CPW) on the PCB was

optimized to eliminate the need for any compensation. The simulated return loss at the signal port for a perfectly $50\ \Omega$ load at the common port of the diplexer (connected to the TWPA) was -17.5 dB at 18 GHz. The final module has four ports, with low- and high-frequency inputs and outputs.

Appendix B: Experimental Setup

The TWPA was cooled to 14 mK with a dilution refrigerator. Each of the device’s four ports was connected to one port of a 4-port micro electromechanical systems (MEMS) switch. These switches were configured to bypass the high-pass and low-pass paths through the TWPA with an SMA thru to calibrate the transmitted power through the device. The switch attached to port 1 of the TWPA (the low-pass input) was also connected to an SNTJ for *in-situ* noise characterization. The TWPA outputs were connected to 20 dB directional couplers so that scattering measurements counter-propagating with the pump could be performed. Finally, each of the outputs was fed into an isolator followed by a high electron mobility transistor (HEMT) amplifier at 4 K. The full testing setup is shown in Fig. 4.

Appendix C: Cryogenic Power Calibration

Knowledge of the power incident on the ports of the TWPA is critical for properly characterizing the 1 dB compression point and the actual pump power. We used the known power spectral density (PSD) S_{in} from the SNTJ to calibrate this power. First, we configured the cryogenic switches to connect the SNTJ directly to the readout chain, bypassing the TWPA using the SMA thru. We measured the output PSD S_{out} at room-temperature for a range of SNTJ biases. It is a function of the known input PSD, S_{in} , and the gain G of the readout chain,

$$S_{\text{out}} = GS_{\text{in}}. \quad (\text{C1})$$

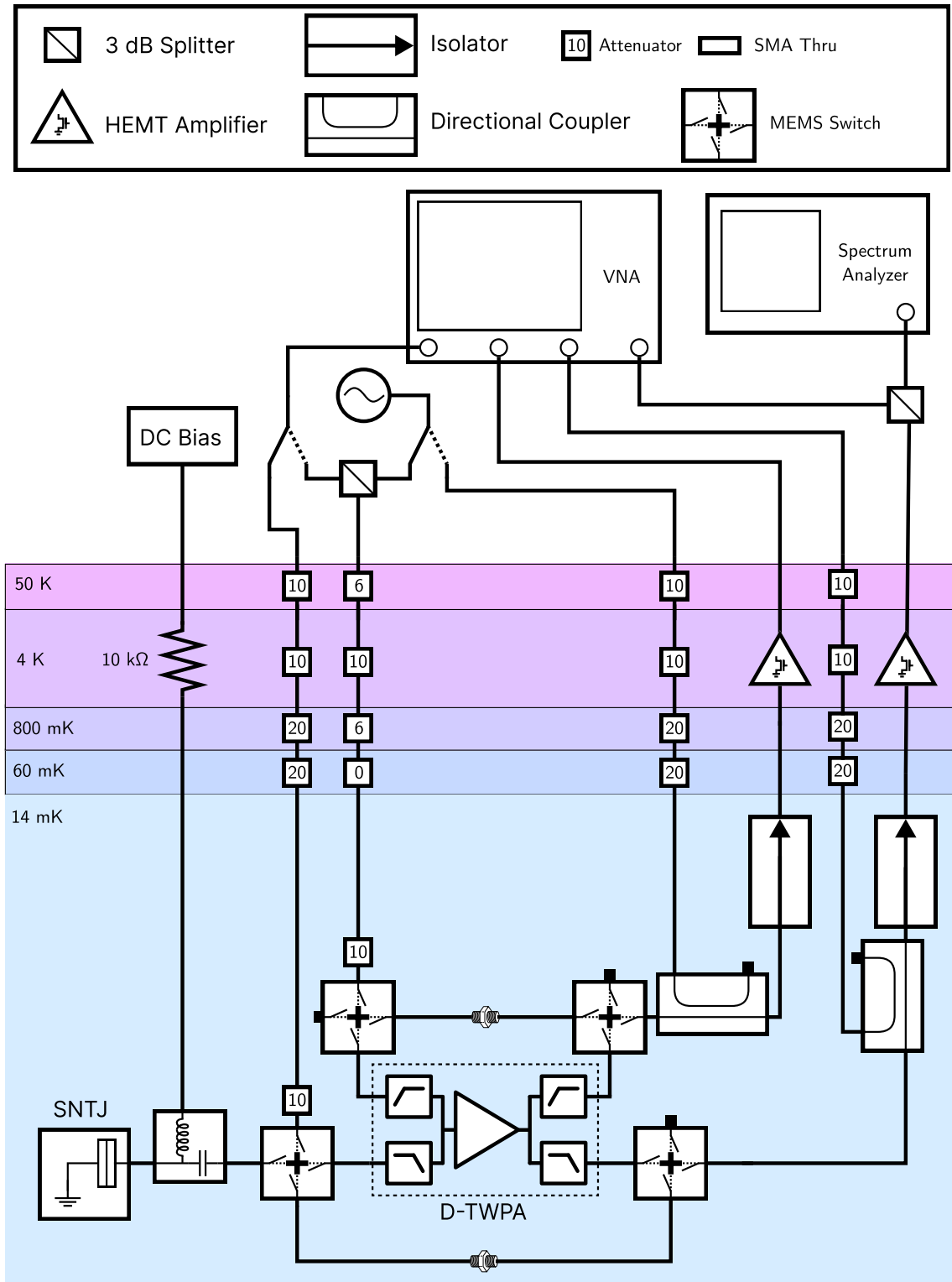


FIG. 4. Full schematic of the experimental setup used to characterize the D-TWPA.

Second, we configured the switches to connect the signal input line to the readout chain again bypassing the TWPA with the thru. We measured S_{out} as a function of VNA power P_{VNA} . This output power, P_{out} , is a function of the gain of the readout chain, G , and of the attenuation A on the input line, from the VNA to the TWPA input:

$$P_{\text{out}} = AGP_{\text{VNA}}. \quad (\text{C2})$$

Combining (C1) and (C2) we can calculate the input line attenuation,

$$A = \frac{P_{\text{out}}}{P_{\text{VNA}}} \frac{S_{\text{in}}}{S_{\text{out}}}. \quad (\text{C3})$$

Generally, this attenuation is a function of frequency, so multiple VNA power sweeps were performed at frequencies between 4 GHz and 9 GHz. The extracted attenuation is shown in Fig. 5. Here, we have neglected the small attenuation (of order 1 dB [14]) existing between the SNTJ output and the TWPA input.

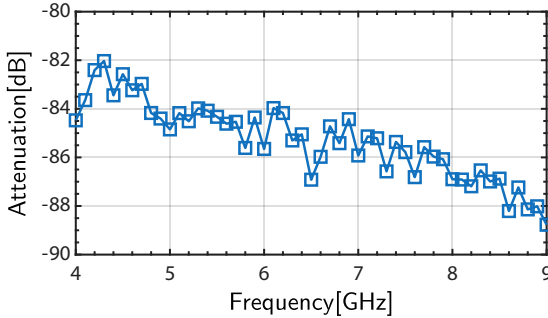


FIG. 5. The calibrated input attenuation as a function of frequency from the VNA to the TWPA input reference plane was determined using the SNTJ as a calibrated power source.

Using this attenuation profile, we can calculate the input 1 dB compression power $P_{1\text{dB}}$ by sweeping the VNA power, shown in Fig. 6.

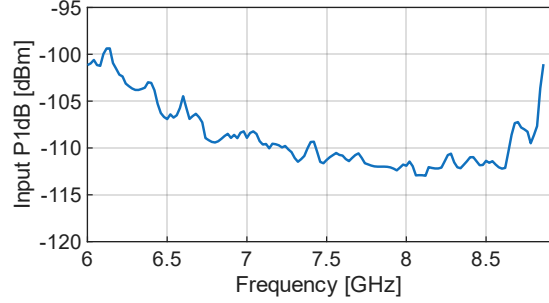


FIG. 6. The 1 dB compression point calculation at 13 dB small-signal gain. The input $P_{1\text{dB}}$ is determined using the input attenuation calibration, Fig. 5, to convert VNA power to power at the TWPA input.

We also used this input attenuation to approximately determine the pump power delivered to the TWPA input: assuming the cryogenic cable assemblies have nearly identical insertion loss and accounting for an additional 28 dB of attenuation on the signal input lines at room temperature, we estimate that the high-pass input line has 61 dB of attenuation at the pump frequency (9.06 GHz), from the VNA to the TWPA input port. Thus, the noise-optimized pump power of -15.8 dBm corresponds to -76.8 dBm at the TWPA input.

Appendix D: Diplexer

The TWPA is connected to the common ports of two identical diplexers. These diplexers are filter networks where the common port (referred to as port 1) directs waves to one of its two other ports (2 and 3) depending on the frequency f of that wave relative to a crossover frequency f_{cx} : ideally, for $f < f_{\text{cx}}$ we may have $S_{21} = 0$ dB while for $f > f_{\text{cx}}$ we may have $S_{31} = 0$ dB. We arranged each of the diplexer's filtering arms in a parallel topology [28], compatible with our CPW topology where the ground planes can then be left continuous and connected everywhere. The TWPA requires a low return loss at all frequencies to avoid self-resonance under pumping, and thus necessitates contiguous-band diplexers, where the end of one passband aligns with the beginning of the next passband at the

crossover frequency f_{cx} . In this configuration, the quality of the match will depend on the filters' orders, and will peak at f_{cx} where it is at best -6 dB, because a 3-port network cannot be simultaneously reciprocal, matched, and lossless [29]. Fortunately, f_{cx} also corresponds to a low TWPA gain region. To design a contiguous-band diplexer we must use singly-terminated filters, whose components are designed for a short circuit on the common port and a load at the source port [28].

We chose singly-terminated, 5th order Chebyshev-I low-pass and high-pass filters with passband ripple $L_{ar} = 0.1$ dB to mitigate fabrication sensitivity, roll-off rate, and design complexity. Since the 3 dB frequency of Chebyshev filters does not correspond to their cutoff frequency, each filter's cutoff needed to be scaled from the $f_{cx} = 8$ GHz crossover frequency by [28]

$$k_n = \cosh \left(\frac{\cosh^{-1} \left(\sqrt{1/\epsilon} \right)}{n} \right), \quad (D1)$$

where $\epsilon = 10^{L_{ar}/10} - 1$, and $n = 5$ is the filter order. Using the normalized component values g_n , we then calculate the actual inductor and capacitor component values. For the low-pass filter,

$$C_{n,low} = \frac{g_n}{Z_0 2\pi f_{c,low}}, \quad (D2)$$

$$L_{n,low} = \frac{g_n Z_0}{2\pi f_{c,low}} \quad (D3)$$

where $f_{c,low} = f_{cx}/k_5$, and where $Z_0 = 50 \Omega$ is the source impedance. Similarly for the high-pass filter,

$$C_{n,high} = \frac{1}{g_n Z_0 2\pi f_{c,high}}, \quad (D4)$$

$$L_{n,high} = \frac{Z_0}{g_n 2\pi f_{c,high}}, \quad (D5)$$

where $f_{c,high} = f_{cx} k_5$. The prototype values and corresponding component values are shown in Tab. I for the filter layout shown in Fig. 7.

g_n	LPF Components	HPF Components
0.573	$L_1 = 0.647$ nH	$C_1 = 0.612$ pF
1.249	$C_2 = 0.564$ pF	$L_2 = 0.702$ nH
1.556	$L_3 = 1.757$ nH	$C_3 = 0.225$ pF
1.592	$C_4 = 0.719$ pF	$L_4 = 0.551$ nH
1.376	$L_5 = 1.553$ nH	$C_5 = 0.255$ pF

TABLE I. Component values in the low-pass and high-pass diplexer arms, calculated from prototype values given in [28].

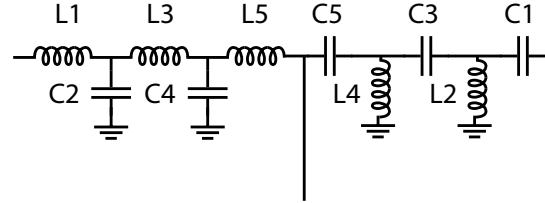


FIG. 7. Component names for the lumped element diplexers.

The layouts of these components were simulated individually, and then integrated into two electromagnetic simulations, one for each filter. These filters were then simulated together and the length between the filters was tuned to achieve the best return loss at the common port near the crossover frequency.

[1] B. Abdo, K. Sliwa, S. Shankar, M. Hatridge, L. Frunzio, R. Schoelkopf, and M. Devoret, Josephson Directional Amplifier for Quantum

Measurement of Superconducting Circuits, *Physical Review Letters* **112**, 167701 (2014).

[2] B. Brubaker, L. Zhong, Y. Gurevich, S. Cahn,

- S. Lamoreaux, M. Simanovskaia, J. Root, S. Lewis, S. Al Kenany, K. Backes, I. Urdinaran, N. Rapidis, T. Shokair, K. Van Bibber, D. Palken, M. Malnou, W. Kindel, M. Anil, K. Lehnert, and G. Carosi, First Results from a Microwave Cavity Axion Search at $24 \mu\text{eV}$, *Physical Review Letters* **118**, 061302 (2017).
- [3] N. Du, N. Force, R. Khatriwada, E. Lentz, R. Ottens, L. Rosenberg, G. Rybka, G. Carosi, N. Woollett, D. Bowring, A. Chou, A. Sonnenschein, W. Wester, C. Boutan, N. Oblath, R. Bradley, E. Daw, A. Dixit, J. Clarke, S. O’Kelley, N. Crisosto, J. Gleason, S. Jois, P. Sikivie, I. Stern, N. Sullivan, D. Tanner, G. Hilton, and ADMX Collaboration, Search for Invisible Axion Dark Matter with the Axion Dark Matter Experiment, *Physical Review Letters* **120**, 151301 (2018).
- [4] J. Heinsoo, C. K. Andersen, A. Remm, S. Krinner, T. Walter, Y. Salathé, S. Gasparinetti, J.-C. Besse, A. Potočnik, A. Wallraff, and C. Eichler, Rapid High-fidelity Multiplexed Readout of Superconducting Qubits, *Physical Review Applied* **10**, 034040 (2018).
- [5] F. Arute, K. Arya, R. Babbush, D. Bacon, J. C. Bardin, R. Barends, R. Biswas, S. Boixo, F. G. S. L. Brandao, D. A. Buell, B. Burkett, Y. Chen, Z. Chen, B. Chiaro, R. Collins, W. Courtney, A. Dunsworth, E. Farhi, B. Foxen, A. Fowler, C. Gidney, M. Giustina, R. Graff, K. Guerin, S. Habegger, M. P. Harrigan, M. J. Hartmann, A. Ho, M. Hoffmann, T. Huang, T. S. Humble, S. V. Isakov, E. Jeffrey, Z. Jiang, D. Kafri, K. Kechedzhi, J. Kelly, P. V. Klimov, S. Knysh, A. Korotkov, F. Kostriksa, D. Landhuis, M. Lindmark, E. Lucero, D. Lyakh, S. Mandrà, J. R. McClean, M. McEwen, A. Megrant, X. Mi, K. Michielsen, M. Mohseni, J. Mutus, O. Naaman, M. Neeley, C. Neill, M. Y. Niu, E. Ostby, A. Petukhov, J. C. Platt, C. Quintana, E. G. Rieffel, P. Roushan, N. C. Rubin, D. Sank, K. J. Satzinger, V. Smelyanskiy, K. J. Sung, M. D. Trevithick, A. Vainsencher, B. Villalonga, T. White, Z. J. Yao, P. Yeh, A. Zalcman, H. Neven, and J. M. Martinis, Quantum supremacy using a programmable superconducting processor, *Nature* **574**, 505 (2019).
- [6] F. Lecocq, L. Ranzani, G. Peterson, K. Cicak, X. Jin, R. Simmonds, J. Teufel, and J. Aumentado, Efficient Qubit Measurement with a Nonreciprocal Microwave Amplifier, *Physical Review Letters* **126**, 020502 (2021).
- [7] E. I. Rosenthal, C. M. Schneider, M. Malnou, Z. Zhao, F. Leditzky, B. J. Chapman, W. Wustmann, X. Ma, D. A. Palken, M. F. Zanner, L. R. Vale, G. C. Hilton, J. Gao, G. Smith, G. Kirchmair, and K. Lehnert, Efficient and Low-Backaction Quantum Measurement Using a Chip-Scale Detector, *Physical Review Letters* **126**, 090503 (2021).
- [8] K. M. Backes, D. A. Palken, S. A. Kenany, B. M. Brubaker, S. B. Cahn, A. Droster, G. C. Hilton, S. Ghosh, H. Jackson, S. K. Lamoreaux, A. F. Leder, K. W. Lehnert, S. M. Lewis, M. Malnou, R. H. Maruyama, N. M. Rapidis, M. Simanovskaia, S. Singh, D. H. Speller, I. Urdinaran, L. R. Vale, E. C. Van Assendelft, K. Van Bibber, and H. Wang, A quantum enhanced search for dark matter axions, *Nature* **590**, 238 (2021).
- [9] S. Krinner, N. Lacroix, A. Remm, A. Di Paolo, E. Genois, C. Leroux, C. Hellings, S. Lazar, F. Swiadek, J. Herrmann, G. J. Norris, C. K. Andersen, M. Müller, A. Blais, C. Eichler, and A. Wallraff, Realizing repeated quantum error correction in a distance-three surface code, *Nature* **605**, 669 (2022).
- [10] M. Malnou, J. A. B. Mates, M. R. Vissers, L. R. Vale, D. R. Schmidt, D. A. Bennett, J. Gao, and J. N. Ullom, Improved microwave SQUID multiplexer readout using a kinetic-inductance traveling-wave parametric amplifier, *Applied Physics Letters* **122**, 214001 (2023).
- [11] C. Macklin, K. O’Brien, D. Hover, M. E. Schwartz, V. Bolkhovskiy, X. Zhang, W. D. Oliver, and I. Siddiqi, A near-quantum-limited Josephson traveling-wave parametric amplifier, *Science* **350**, 307 (2015).
- [12] L. Planat, A. Ranadive, R. Dassonneville, J. Puertas Martínez, S. Léger, C. Naud, O. Buisson, W. Hasch-Guichard, D. M. Basko, and N. Roch, Photonic-Crystal Josephson Traveling-Wave Parametric Amplifier, *Physical Review X* **10**, 021021 (2020).
- [13] M. Malnou, M. Vissers, J. Wheeler, J. Aumentado, J. Hubmayr, J. Ullom, and J. Gao, Three-Wave Mixing Kinetic Inductance Traveling-Wave Amplifier with Near-Quantum-Limited Noise Performance, *PRX Quantum* **2**, 010302 (2021).
- [14] M. Malnou, T. F. Q. Larson, J. D. Teufel, F. Lecocq, and J. Aumentado, Low-noise cryogenic microwave amplifier characterization with a calibrated noise source, *Review of Scientific Instruments* **95**, 034703 (2024).
- [15] M. Malnou, B. T. Miller, J. A. Estrada, K. Gen-

- ter, K. Cicak, J. D. Teufel, J. Aumentado, and F. Lecocq, A travelling-wave parametric amplifier and converter, *Nature Electronics* **8**, 1082 (2025).
- [16] A. Ranadive, B. Fazliji, G. Le Gal, G. Cappelli, G. Butseraen, E. Bonet, E. Eyraud, S. Böhling, L. Planat, A. Metelmann, and N. Roch, A travelling-wave parametric amplifier isolator, *Nature Electronics* **8**, 1089 (2025).
- [17] L. Spietz, K. W. Lehnert, I. Siddiqi, and R. J. Schoelkopf, Primary Electronic Thermometry Using the Shot Noise of a Tunnel Junction, *Science* **300**, 1929 (2003).
- [18] L. Spietz, R. J. Schoelkopf, and P. Pari, Shot noise thermometry down to 10mK, *Applied Physics Letters* **89**, 183123 (2006).
- [19] Su-Wei Chang, J. Aumentado, Wei-Ting Wong, and J. C. Bardin, Noise measurement of cryogenic low noise amplifiers using a tunnel-junction shot-noise source, in *2016 IEEE MTT-S International Microwave Symposium (IMS)* (IEEE, San Francisco, CA, 2016) pp. 1–4.
- [20] O. Yaakobi, L. Friedland, C. Macklin, and I. Siddiqi, Parametric amplification in Josephson junction embedded transmission lines, *Physical Review B* **87**, 144301 (2013).
- [21] K. O’Brien, C. Macklin, I. Siddiqi, and X. Zhang, Resonant Phase Matching of Josephson Junction Traveling Wave Parametric Amplifiers, *Physical Review Letters* **113**, 157001 (2014).
- [22] F. Lecocq, L. Ranzani, G. Peterson, K. Cicak, R. Simmonds, J. Teufel, and J. Aumentado, Non-reciprocal Microwave Signal Processing with a Field-Programmable Josephson Amplifier, *Physical Review Applied* **7**, 024028 (2017).
- [23] K. Peng, M. Naghiloo, J. Wang, G. D. Cunningham, Y. Ye, and K. P. O’Brien, Floquet-Mode Traveling-Wave Parametric Amplifiers, *PRX Quantum* **3**, 020306 (2022).
- [24] J. Wang, K. Peng, J. M. Knecht, G. D. Cunningham, A. E. Lombo, A. Yen, D. A. Zaidenberg, M. Gingras, B. M. Niedzielski, H. Stickler, K. Sliwa, K. Serniak, M. E. Schwartz, W. D. Oliver, and K. P. O’Brien, High-efficiency, low-loss floquet-mode traveling wave parametric amplifier (2025), [arXiv:2503.11812 \[quant-ph\]](https://arxiv.org/abs/2503.11812).
- [25] Whiteley Research Inc., WRSpice Circuit Simulation Program, <http://www.wrcad.com> (2025), sunnyvale, CA.
- [26] V. Gaydamachenko, C. Kissling, and L. Grünhaupt, rf-SQUID-based traveling-wave parametric amplifier with input saturation power of -84 dBm across more than one octave in bandwidth, *Physical Review Applied* **23**, 064053 (2025).
- [27] C. S. Chang, A. F. Van Loo, C.-C. Hung, Y. Zhou, C. Gnannt, S. Tamate, and Y. Nakamura, Josephson traveling-wave parametric amplifier based on a low-intrinsic-loss lumped-element coplanar waveguide, *Physical Review Applied* **24**, 044081 (2025).
- [28] G. L. Matthaei, L. Young, and E. M. T. Jones, *Microwave filters, impedance-matching networks, and coupling structures*, facsim. ed ed., The Artech house microwave library (Artech, Dedham (Mass.), 1980).
- [29] R. E. Collin, *Foundations for microwave engineering*, second edition ed., IEEE Press series on electromagnetic wave theory (IEEE Press, Wiley-Interscience, New York Hoboken, New Jersey, 2001)